

Waves and instability in a one-dimensional microfluidic array

Bin Liu, J. Goree, and Yan Feng

Department of Physics and Astronomy, The University of Iowa, Iowa City, Iowa 52242

(Received 12 July 2012; revised manuscript received 5 September 2012; published 11 October 2012)

Motion in a one-dimensional (1-D) microfluidic array is simulated. Water droplets, dragged by flowing oil, are arranged in a single row. Due to their hydrodynamic interactions, the spacing between these droplets oscillates with a wave-like motion that is longitudinal or transverse. The simulation yields wave spectra that agree well with experiment. The wave-like motion has an instability which is confirmed to arise from nonlinearities in the interaction potential. The instability's growth is spatially localized. By selecting an appropriate correlation function, the interaction between the longitudinal and transverse waves is described.

DOI: [10.1103/PhysRevE.86.046309](https://doi.org/10.1103/PhysRevE.86.046309)

PACS number(s): 47.55.D-, 47.60.-i, 47.20.Ky, 63.22.-m

I. INTRODUCTION

Flows at a micron scale, called microfluidic flows, are of interest in fields such as molecular analysis, molecular biology and microelectronics [1]. Some microfluidic flows include a dispersed phase, such as droplets, bubbles, biological cells, or colloidal particles. In microfluidics, there is a flow in a channel that has at least one dimension that is hundreds of microns or smaller. In such a channel, a dispersed phase such as water droplets can be made to align in an array consisting of a single row, as sketched in Fig. 1; structures like these have been termed a one-dimensional (1-D) array [3,4], a 1-D stream [5], or a 1-D crystal [6–8]. Such 1-D arrays have applications in protein crystallization [3,4] and flow cytometry [9], and they can exhibit physical phenomena such as waves [5–8] and instabilities [6–8,10].

In this paper, we report a numerical simulation that mimics the experiment of Beatus *et al.* [6]. In that experiment, a 1-D array of water droplets was dragged by a flow of oil in a microfluidic channel, as sketched in Fig. 1. Due to the friction they experienced on the floor and ceiling of the channel, the water droplets moved more slowly than the oil. As they were injected into the oil flow, the water droplets at first self-organized in a single row with a highly regular spacing along the centerline of the channel. The authors described this regularly spaced array of droplets as a 1-D crystal. One discovery in the experiment of Beatus *et al.* was that the droplets fluctuate about their unperturbed crystal positions with a wave-like motion that was surprisingly not overdamped by viscous dissipation. This wave-like motion, termed phonon by the experimenters, included displacements in two directions with respect to the flow, parallel and perpendicular, corresponding to longitudinal and transverse waves, respectively. Another finding in the experiment was an instability that developed farther downstream. This instability, in which a local fluctuation grew to a large amplitude, was attributed by the experimenters to nonlinear effects due to two factors: large amplitude motion and an interaction between longitudinal and transverse waves. Eventually, the 1-D structure was destroyed by an extreme transverse displacement of droplets that allowed them to move past another in the longitudinal direction. The system of droplets was driven out of equilibrium by the imposed flow of oil, which was also the energy source for phonons and instabilities in the system [6].

The wave motion and instability in the dispersed phase were described by Beatus *et al.* [6–8] as the result of hydrodynamic interaction. One droplet disturbs the surrounding flow, which in turn disturbs another droplet via a drag force on the droplet due to the relative velocity between the faster oil and the slower droplet. Manifestations of this kind of hydrodynamic interaction have been reported for other microfluidic flows; these include self-assembly patterns [11–13], shock waves [5,8], and oscillatory waves. The latter were discovered experimentally by Beatus *et al.* [6,8] and studied in simulations where the flow field, scattered by droplets or particles, is modeled as a superposition of the far fields of dipoles [6,8] or is calculated by a Stokesian-dynamics method [14].

As in Refs. [6,8], our simulation treats individual droplets as particles that move according to a well-defined equation of motion. Instead of computing the entire flow field for the oil, we model the hydrodynamic interactions in the droplets' equation of motion. The model we use for the hydrodynamic interactions was developed theoretically by Beatus *et al.* [6,8], who treated the oil flow as a potential flow.

The simulation we report here shows agreement with the wave spectrum, dispersion relation, and instability in the experiment [6]. We use the simulation to verify that the instability is due to nonlinearity, as proposed by Beatus *et al.* [6]. We also use the simulation results to describe the interaction of the longitudinal and transverse waves; we do this by selecting an appropriate correlation function based on the time series of the longitudinal and transverse microscopic currents.

The physics that will be studied here, in a 1-D microfluidic array, is also relevant to other physical systems that have a single row of particles or atoms. These systems include a line of colloidal microspheres confined by holographic optical traps [15], a line of charged micron-sized particles levitated in dusty plasmas [16,17], and a line of helium atoms adsorbed on bundles of single-walled carbon nanotubes [18]. In these examples, the particles require some mechanism to confine them so that they form a 1-D array, and the collection of particles can sustain wave-like motion due to a combination of the confinement and the interaction between the particles.

II. SIMULATION

We simulate a 1-D array of water droplets with the same configuration and parameters as in the experiment of Beatus

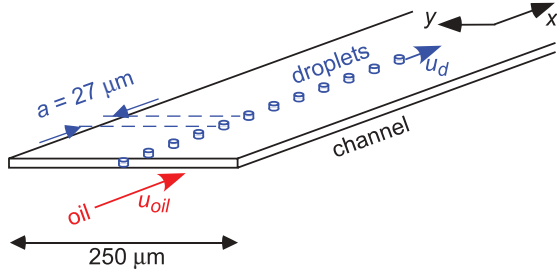


FIG. 1. (Color online) Sketch of a 1-D array of water droplets dragged slowly by a faster flow of oil in a microfluidic channel, as in the experiment of Ref. [6], which had a height of $10 \mu\text{m}$. The droplets are approximated as having a cylindrical disk shape, with a radius of $R = 10 \mu\text{m}$. In the experiment, there was probably a thin layer of oil and surfactant that provides a lubricating effect between water droplets and the surfaces of the floor and ceiling of the channel [2].

et al. [6]. As sketched in Fig. 1, the channel is aligned in the x direction and the droplet's radius is $R = 10 \mu\text{m}$. The simulation begins after water droplets have been injected, so that they are initially spaced by $a = 27 \mu\text{m}$. In calculating the forces acting on the droplets, we assume an oil flow velocity of $u_{\text{oil}}^{\infty} = 1730 \mu\text{m/s}$, while the droplets move more slowly, at $u_d = 380 \mu\text{m/s}$.

We numerically integrate the equations of motion of all the simulated droplets. A droplet is treated individually as a point object that responds to hydrodynamic forces, which are calculated to take into account of the finite radius R of the flattened droplet. The equation of motion for the n th droplet, modeled for a potential flow, is [6]

$$\frac{d\mathbf{r}_n}{dt} = \frac{u_d}{u_{\text{oil}}^{\infty}} \nabla \phi(\mathbf{r}_n), \quad (1)$$

where ϕ is the flow potential. This equation of motion expresses a balance of two forces: the friction on the channel walls and the drag in the oil flow. Equation (1) includes only hydrodynamic effects; other effects such as fluctuating Brownian motion due to the discreteness of molecules in the oil or water are neglected. The inertial term in Newton's second law is also neglected, so that unlike some equations of motion, Eq. (1) is a first-order differential equation. For each droplet, we integrate the equation of motion, so that the position \mathbf{r}_n and velocity $d\mathbf{r}_n/dt$ of all the droplets are advanced simultaneously in a sequence of time steps.

As in Ref. [6], we model the potential ϕ as

$$\phi(\mathbf{r}) = u_{\text{oil}}^{\infty} x + \sum_m \phi_d(\mathbf{r} - \mathbf{r}_m), \quad (2)$$

where the first term on the right is a potential due to oil flowing uniformly at u_{oil}^{∞} and the second term (which is sometime positive and sometime negative) is a superposition of the potentials due to all other droplets m . An underlying assumption in Eq. (2) is that the droplet phase can be modeled by a pairwise interaction. As in Ref. [6], for the pairwise interaction potential ϕ_d , we use

$$\phi_d(\mathbf{r}) = R^2 (u_{\text{oil}}^{\infty} - u_d) \frac{x}{r^2}, \quad (3)$$

which is the potential due to a dipole aligned with the flow in the \hat{x} direction. Here, $r = \sqrt{x^2 + y^2}$ is the distance from the droplet located at $x = 0$, $y = 0$. Equation (3) assumes that the droplet has been flattened by the channel to have the shape of a thin disk, and that the surrounding flow has a Poiseuille-like parabolic profile along the z axis and can be described in the xy plane as a potential flow, as in a Hele-Shaw cell. Equation (3) also assumes that the droplets are unconfined in the xy plane; that is, we assume that the channel width is so great that its effects can be neglected. Such finite width effects could be accounted for by using a different potential [7,8].

The force, which varies as $-\nabla\phi$ on the right-hand-side of Eq. (1), is nonlinear with respect to displacements of a droplet when using Eqs. (2) and (3) to describe ϕ . Most of our results are for this nonlinear case. However, in Sec. III C3 we will perform a test with a linearized form of $-\nabla\phi$. This linearized form is obtained by performing a Taylor expansion of Eq. (3) for small displacements δx and δy from an equilibrium position x_0 , where $x = x_0 + \delta x$ and $y = \delta y$. This expansion of Eq. (3) is

$$\phi_d(x, y) \approx \frac{R^2 (u_{\text{oil}}^{\infty} - u_d)}{x_0} \left[1 - \frac{\delta x}{x_0} + \left(\frac{\delta x}{x_0} \right)^2 - \left(\frac{\delta y}{x_0} \right)^2 + \text{h.o.t.} \right]. \quad (4)$$

To turn off nonlinear effects in $-\nabla\phi$, we can retain only the first four terms in the brackets and neglect the higher-order terms (h.o.t.); we will do this only in Sec. III C3. For all other results, we will use the fully nonlinear force computed using Eq. (3) instead.

Our simulation includes $N = 256$ droplets, and we use a periodic boundary condition [19,20] to mimic the behavior of an infinite 1-D array. We apply the periodic boundary condition only in the x direction. With this boundary condition, for example, a droplet exiting the simulation box from the left-hand side will reenter the box from the right-hand side. The calculation of the potential ϕ in Eq. (2) is summed over not only the 256-droplet cell, but also over "image cells" that repeat on each side. The use of periodic boundary conditions in molecular dynamics simulations typically requires either cutting off the interaction potential at large distance or using Ewald potentials [19]. The Ewald potential approach is generally used for slowly decaying potentials, such as a $1/r$ Coulomb potential, to avoid systematic errors in the total potential energy for the system [19]. Although our potential ϕ_d as given by Eq. (3) decays as $1/r$, we chose not to use Ewald potentials, but instead use a large cutoff radius so that ϕ_d is replaced by zero for $r > r_{\text{cut}}$ where we chose $r_{\text{cut}} = 64a$. To validate this choice, we performed a series of tests to determine that the cutoff radius and system size were large enough not to cause any noticeable deviation in the quantities that we report. These tests included increasing the system size to as large as $N = 4096$ and the cutoff radius as large as $r_{\text{cut}} = 512a$. We found that the quantities reported in this paper (including mean squared velocity of droplets, wave spectral power, and current correlation function) are not noticeably affected by varying N or r_{cut} in these tests, thereby giving us confidence in our use of the cutoff radius.

The simulation is performed by integrating the droplets' equation of motion in the inertial frame of the droplets. To imitate the confinement provided by the floor and ceiling of the channel, the droplet is constrained to have no movement in the vertical direction, so that the equation of motion is integrated in only two coordinates, x and y . The simulation runs until two droplets touch, which occurs after approximately 10 s. Our approximations for the interaction may be less accurate when two droplets are close enough to touch, so we stop our simulation when this first occurs. To advance a droplet's position, we use a fourth-order Runge-Kutta integrator with a fixed time step [21]. The time step was selected as 5.6×10^{-5} s by performing a test requiring that unphysical changes in the sum of the squared velocities of droplets are negligible over the simulation's duration.

Because the droplets in the 1-D array are allowed to move in two directions, perpendicular and parallel to the flow, the 1-D array can sustain two modes, longitudinal and transverse, respectively. Due to the finite number of droplets, small-amplitude motion can be decomposed into 256 discrete sinusoidal modes for the longitudinal motion, and the same for the transverse motion. Thus, the allowed values of ka in our simulation are $\pm\pi/128, \pm2\pi/128, \dots, \pm\pi$, where $a = 27 \mu\text{m}$ is the equilibrium spacing (lattice constant), and $k = 2\pi/\lambda$ is the wave number for a mode of wavelength λ .

Our initial conditions at $t = 0$ are chosen to mimic small random displacements of the droplets from their unperturbed crystal positions. We start a droplet m at a position $x_m = (m - N/2 + \delta_x)a$ and $y_m = \delta_y a$. Here, δ_x and δ_y are random numbers, with a mean of zero and a standard deviation [22] of 0.01. The random numbers, which were different for each droplet, were chosen so that there would initially be equal spectral power in each of the 256 longitudinal and 256 transverse modes. (This was done by initially giving each mode the same amplitude, but with a random phase.) We performed

multiple runs with different sequences of random numbers for the initial conditions.

After running the simulation and obtaining time series of the positions and velocities of all droplets, we use time series data for the longitudinal position x_m and the velocities $v_{x,m}$ and $v_{y,m}$ for each droplet m to calculate

$$j_L(k, t) = \sum_{m=1}^N v_{x,m}(t) e^{-ikx_m(t)} \quad (5)$$

and

$$j_T(k, t) = \sum_{m=1}^N v_{y,m}(t) e^{-ikx_m(t)}. \quad (6)$$

Equations (5) and (6) describe the fluctuating velocities of droplets in the longitudinal (\hat{x}) and transverse (\hat{y}) directions, respectively, for a specified value of the wave number k . In the literature for the physics of liquids, j_L and j_T are sometimes called ‘‘microscopic currents’’ [23], which can characterize the oscillatory wave-like motion of molecules in a liquid. Here, instead of molecules, we track the motion of droplets. We compute the currents for all 256 longitudinal and 256 transverse modes that are allowed for our simulation.

III. RESULTS

A. Droplet positions and velocities

In Fig. 2 we present raw simulation data consisting of positions recorded at three times. At $t = 0$ the simulation's initial conditions are shown, with droplets located almost at equal spacing a along the centerline of the channel, with small random displacements in both x and y , as described in Sec. II. At $t = 5$ s, the displacements of the droplets have

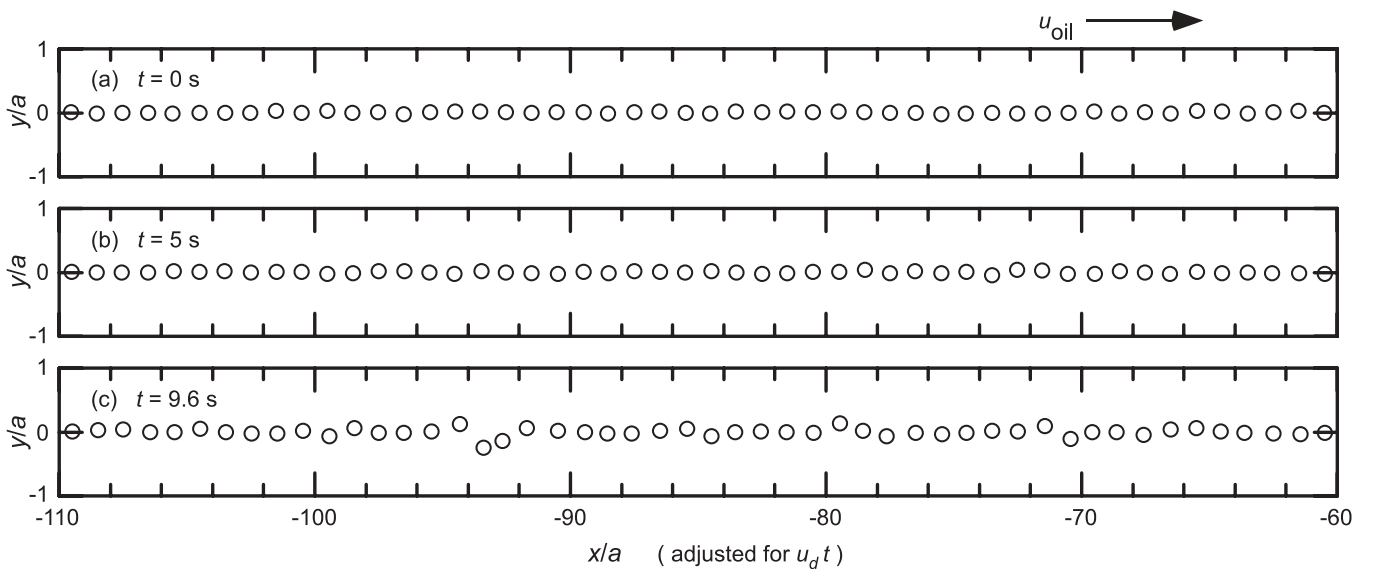


FIG. 2. Droplet positions, at three times in the simulation, shown in the inertial frame of the array of droplets. Only a portion of a total of 256 droplets is shown here. (a) At the time $t = 0$, the initial positions of the droplets are specified. We then integrate the fully nonlinear equation of motion, Eqs. (1)–(3), to advance the droplet position and velocity each time step. (b) At $t = 5$ s, a droplet fluctuates about its equilibrium position. (c) At $t = 9.6$ s, the displacements of the droplets have grown as large as a , due to the instability.

become large enough to be easily detected by our diagnostics, although they are still too small to be identified in a visual inspection of Fig. 2. At the end of the simulation, $t = 9.6$ s, the displacements of the droplets have grown as large as a due to the instability. At the position $x/a \approx -94$ in Fig. 2 (c), we observe a fluctuation resembling the 1 + 3 arrangement of droplets observed in the experiment [6,8] and in the simulation of Beatus *et al.* [8]. Eventually, after about 5 to 12 s depending on the simulation run, the droplets move past one another (i.e., change their sequence), and at that point in the development of the instability, the 1-D lattice structure is essentially broken. For run 1, which provides most of the data for this paper, this breaking occurs at $t \approx 10$ s. The three panels shown in Fig. 2 are representative of the entire simulation movie, which we provide in the Supplemental Material [24].

We will use the raw data for droplet positions and velocities, and the currents computed from them using Eqs. (5) and (6), as the inputs to several diagnostics to characterize the waves and instability, as described next.

B. Waves

1. Wave spectra

In Fig. 3 we present the wave spectra, which characterize wave-like motion in the 1-D array of water droplets. These spectra were prepared by computing fast Fourier transforms (FFT) of the currents $j_L(k,t)$ and $j_T(k,t)$ with respect to time for each allowed k and then plotting the spectral power (the square of the modulus of the FFT) as a function of k and frequency ω . In physical systems in which the inertia term in the equation of motion is significant, the spectral power is often considered as being related to kinetic energy; in this system, however, the inertial term is neglected, so that we do not explicitly relate the spectral power to kinetic energy.

We find that our wave spectra in Fig. 3 agree with the experimental spectra [6]. The most obvious difference is that

our spectra do not include a feature due to fabrication defects in the channel that deflected the droplet motion in the experiment.

a. Dispersion relation. For both the longitudinal wave in Fig. 3(a) and the transverse wave in Fig. 3(b), the spectral power is strongest along a curve in the ω and k parameter space. This variation of the resonance frequency with wave number indicates the wave dispersion relation.

For comparison, we also show in Fig. 3 the theoretical dispersion relation derived in Ref. [6] from a linearized equation of motion for small-amplitude motion with a dipole interaction

$$\begin{aligned}\omega_L(k) &= -\frac{6C_s}{\pi^2 a} \sum_m \frac{\sin(mka)}{m^3}, \\ \omega_T(k) &= \frac{6C_s}{\pi^2 a} \sum_m \frac{\sin(mka)}{m^3}.\end{aligned}\quad (7)$$

We calculated the dispersion relation curves for this linear theory using the experimental values of the droplet spacing a and sound velocity $C_s \simeq [2\pi^2 R^2 u_d / (3a^2 u_{oil}^\infty)](u_{oil}^\infty - u_d)$, with no free parameters. We find that the dispersion relation for the linear theory accurately matches our simulation results.

The two waves propagate in opposite directions. In the inertial frame of the droplets, the transverse wave propagates in the $+x$ direction (i.e., in the same direction as the oil flow), while the longitudinal wave propagates in the $-x$ direction (opposite to the oil flow). These directions of propagation can be identified in Fig. 3 by noting that for small $|ka|$, the phase velocities $v_\phi = \omega/k$ of transverse and longitudinal waves are positive and negative, respectively. These wave directions are the same as was observed in the experiment [6].

We find that the power in our spectra is not equally partitioned among the possible values of wave number k . In our simulation, the power becomes concentrated in a range of wave numbers, $ka \approx \pm\pi/2$, which is near the maximum frequency. We will comment upon the significance of $ka \approx \pm\pi/2$ later.

b. Feature not predicted by linear theory. Although the dispersion relations observed in our simulation agree with the

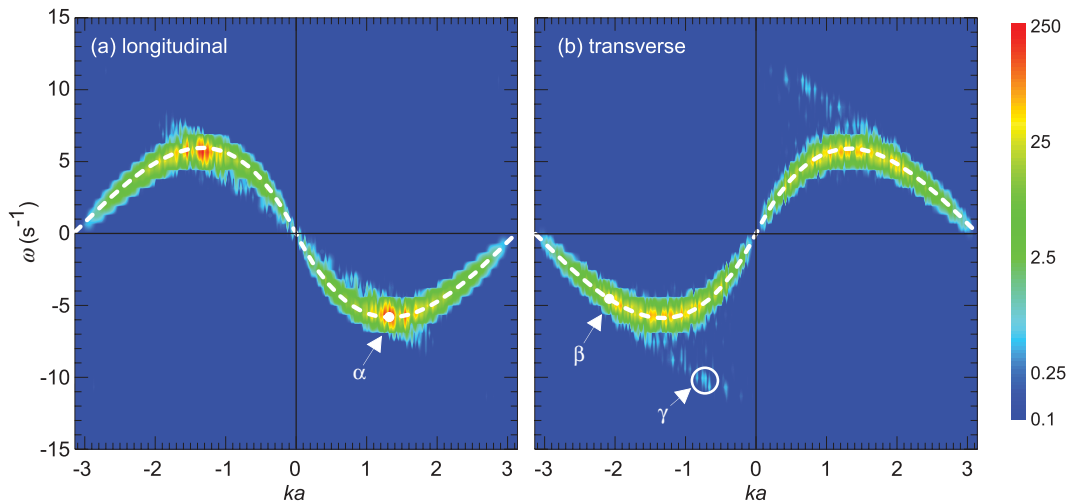


FIG. 3. (Color online) Power spectra of longitudinal (a) and transverse (b) waves, with the logarithm of spectral power shown as a function of frequency and wave number. Spectral power is mostly concentrated in narrow ranges, which are centered on the dispersion relations for a linear theory [Eq. (7)], shown as dashed lines. The feature near $ka \approx \pm 0.8$ and $\omega \approx \pm 10$ s $^{-1}$, marked γ in (b), is not predicted by the linear theory and is interpreted here as an indication of nonlinear effects, possibly resonant wave interaction of the waves marked α and β .

linear theory, we also observe a weaker feature that is not predicted by the linear theory of Eq. (7). This feature is seen near $ka \approx \pm 0.8$ and $\omega \approx \pm 10 \text{ s}^{-1}$, where it is marked γ in Fig. 3(b). Because these modes are not expected from a linear theory, there must be some nonlinear effects involved.

Beatus *et al.* [6] suggested that nonlinearity arose in their experiment due to two factors: large-amplitude motion and an interaction of the longitudinal and transverse waves. This suggestion motivates us to consider what type of wave-wave interaction it could be.

One possible type of nonlinear interaction is the generation of a third wave due by nonlinear mixing of two other waves obeying the criteria

$$\omega_1 + \omega_2 = \omega_3, \quad (8)$$

and

$$k_1 + k_2 = k_3. \quad (9)$$

Such a process is called by various names: “resonant wave interaction” in fluid mechanics [25], “parametric decay” in plasma physics [26], and “three-wave mixing” in optics [27]. We will use the terminology “resonant wave interaction.” An argument in favor of our resonant wave interaction hypothesis is that the ω and k of the longitudinal waves marked α in Fig. 3 and the transverse waves marked β add up to match those of the feature marked γ , as in Eqs. (8) and (9). However, feature γ does not lie on an allowed dispersion relation for linear waves, unlike the best known cases of the resonant wave interaction in fluid mechanics [25] and the three-wave mixing in plasma physics [26]. Further work is needed to test this resonant wave interaction hypothesis.

2. Wave correlation

Having found in Fig. 3 a possible indication of nonlinear coupling of the longitudinal and transverse waves in the spectra, we now seek another diagnostic to indicate any interaction or synchronization of these two waves. Using the longitudinal and transverse currents, $j_L(k_L, t)$ and $j_T(k_T, t)$, respectively, we calculate a correlation function

$$C_{LT}(k_L, k_T, \tau) = \frac{\langle j_L(k_L, t) j_T(k_T, t + \tau) \rangle}{\sqrt{\langle |j_L(k_L, t)|^2 \rangle \langle |j_T(k_T, t)|^2 \rangle}}. \quad (10)$$

In Eq. (10), τ is a time delay, and $\langle \dots \rangle$ is an average over time t . The time interval for the averaging was selected to be as large as possible, given the 10 s duration of our simulation. The correlation function C_{LT} is a complex number; we will report its modulus

$$|C| \equiv |C_{LT}(k_L, k_T, 0)|, \quad (11)$$

as a measure of the strength of the correlation between the two waves. For steady conditions, a value $|C| = 1$ would indicate perfect correlation (although we should note that the conditions here are not steady, due to the growth of the instability). Since we are investigating whether a longitudinal wave and a transverse wave are correlated, we present $|C|$ as a function of the longitudinal wave number k_L and transverse wave number k_T (Fig. 4).

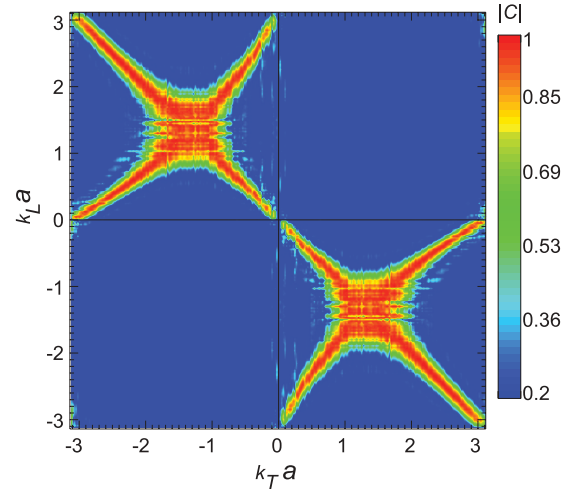


FIG. 4. (Color online) Correlation strength $|C|$, as defined in Eq. (11), for longitudinal k_L and transverse k_T waves. We find a strong correlation, for certain combinations of k_L and k_T . The contour scale has a threshold of 0.2 to suppress noise.

The results in Fig. 4 indicate a significant correlation of the longitudinal and transverse waves. This is evident from the dark regions in Fig. 4, which indicate a high correlation $|C|$.

To help interpret the correlation data in Fig. 4, we present Fig. 5 to indicate the conditions of highest correlation. We find that high correlations occur for waves that obey a matching condition for wave number, which is either

$$k_L = -k_T \quad (12)$$

or

$$k_L a = k_T a \pm (\pi - \epsilon), \quad (13)$$

where $0 \leq \epsilon < 0.5$. As we will see later, ϵ varies with wave number.

We also find that the waves with high correlation obey a matching condition for frequency

$$\omega_L = \omega_T. \quad (14)$$

To demonstrate this matching condition, we combine the dependence of our correlation on wave number and the theoretical dispersion relations [Eq. (7)], which are graphed on the edges of the main panel of Fig. 5. In examining Fig. 5, one can start with the open circle on the longitudinal dispersion relation, and then follow dashed line $H1$ to the left, where it is seen to have high correlations with two wave numbers for transverse waves, as indicated by vertical lines $V1$ and $V2$. All three of these modes (indicated by open and solid circles) have the same frequencies. This observation leads us to the frequency matching condition, Eq. (14). As shown in Appendix, we find that the wave number dependence of ϵ in Eq. (13) can be approximated as

$$\epsilon(k_T) = [(2.309\pi)^2 - (k_T a + 2.058)^2]^{1/2} + k_T a - 1.058\pi, \quad (15)$$

for $-\pi \leq k_T a \leq 0$, and

$$\epsilon(k_T) = [(2.309\pi)^2 - (k_T a - 2.058)^2]^{1/2} - k_T a - 1.058\pi, \quad (16)$$

for $0 \leq k_T a \leq \pi$.

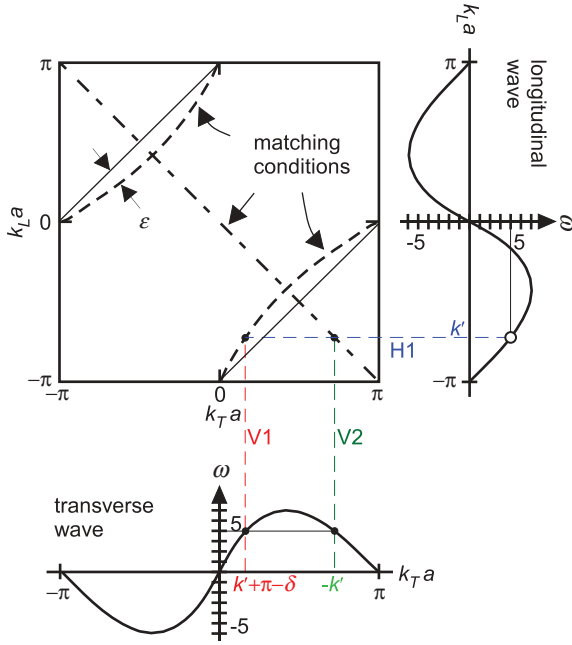


FIG. 5. (Color online) Interpretation of correlation data in Fig. 4. Wave numbers that exhibit high correlations in Fig. 4 obey matching conditions for wave numbers shown with a dot-dash curve with $k_L a = -k_T a$ and dashed curves with $k_L a = k_T a \pm (\pi - \epsilon)$ where $0 \leq \epsilon < 0.5$. We also find a matching condition for frequency by comparing to the dispersion relations, Eq. (7), which are plotted along the edges of the correlation graph. As an example of these matching conditions, we consider a longitudinal wave k' as marked with an open circle. Following the horizontal line $H1$ across the diagram, strong correlation occurs for the transverse waves with wave numbers $-k'$ and $k' + \pi - \delta$, which have the same frequency as the longitudinal wave.

While our correlation function indicates a significant correlation, it does not explain the mechanism for this correlation. This is, of course, a common limitation of using correlation functions.

3. Wave fronts

To visualize the spatiotemporal characteristics of the wave fronts, we present in Fig. 6 a spacetime diagram, which is a plot of droplet velocity as a function of position x and time t . We prepared this spacetime diagram by combining the time series for position $x(t)$ and one component of the velocity, for example $v_x(t)$, to generate contours of constant v_x in the parameter space x vs t . A darker shade in Fig. 6 indicates a higher droplet speed. These spacetime diagrams are useful for characterizing the spatiotemporal development of the droplet motion over the course of the entire simulation.

Features that can be seen in the spacetime diagram include wave fronts for the longitudinal and transverse waves. These wave fronts appear as sloped stripes. For long wavelengths, the longitudinal waves propagate in the $-x$ direction, while the transverse waves propagate in the $+x$ direction, so that these two kinds of wave fronts are sloped oppositely in Fig. 6.

The observed phase velocity v_ϕ of the waves is found by measuring the slope of the wave fronts in the spacetime diagram. We find that $v_\phi = -100 \mu\text{m/s}$ for the longitudinal and $v_\phi = 100 \mu\text{m/s}$ for the transverse waves. These observed phase velocities correspond to $|v_\phi| = |\omega/k|$ evaluated near $ka \approx \pm\pi/2$. As sketched in Fig. 7, the phase velocity depends on wave number. The observed phase velocities are significantly slower than the sound speed, $C_s = 250 \mu\text{m/s}$, for the waves with smaller k . Our observation that the observed phase velocity is dominated by waves at $ka \approx \pm\pi/2$ further indicates that the motion of droplets is dominated by the wave modes near the maximum frequencies, as we saw from the concentration of the wave power near $ka \approx \pm\pi/2$ in the wave spectra of Fig. 3.

C. Instability

We now present our results for the instability. We will find that the instability grows nonexponentially, with a distinctive spatial localization. We will also confirm that the instability requires: (1) nonlinearity in the forces and (2) a coupling between longitudinal and transverse motions.

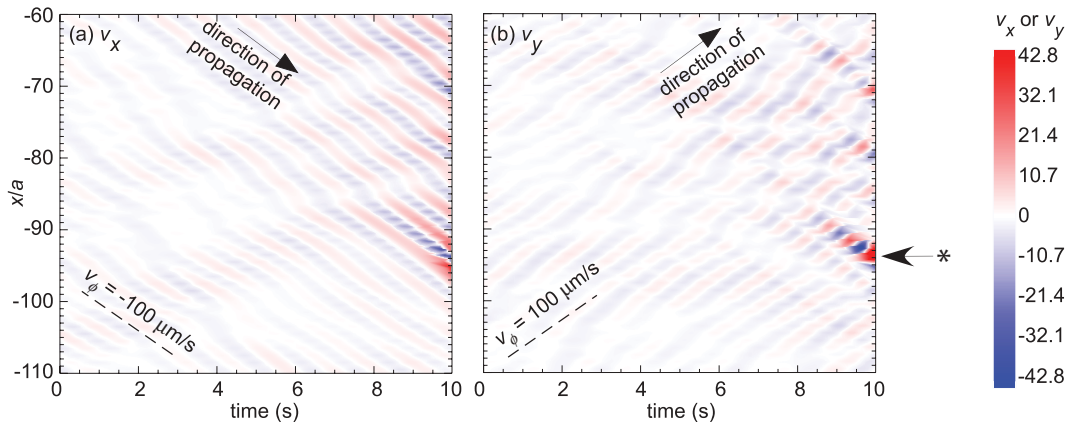


FIG. 6. (Color online) Space-time diagrams for velocities (a) v_x and (b) v_y . To make the spacetime diagram easier to examine, we present the data for only a portion of the array of droplets, $146 \leq m \leq 196$. The sloped stripes in (a) and (b) indicate that longitudinal and transverse wave packets propagate in opposite directions. Note that the wave growth is spatially localized and that the high-amplitude wave packets at $t > 8$ s include only three or four droplets at the location marked $*$.

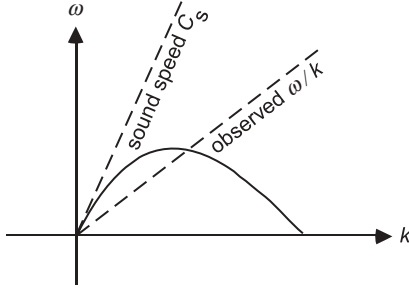


FIG. 7. Sketch of dispersion relation. The slope, which corresponds to the phase speed ω/k , varies with k because of the curvature of the dispersion relation. Two cases of interest are shown: for long wavelength (small k), ω/k is the sound speed $C_S = 250 \mu\text{m/s}$, while for a shorter wavelength (larger k), ω/k is slower. In Fig. 6 we observe a phase speed of $100 \mu\text{m/s}$, corresponding to the lesser slope indicated here.

1. Temporal growth

A feature that can be seen in the spacetime diagram of Fig. 6 is a growth trend for the amplitude of the waves. As time progresses, the velocity amplitudes of both the longitudinal and transverse waves grow, as indicated by the shading in Fig. 6 appearing darker at larger times.

To reveal the scaling of the growth with time, we can also examine a time series of the mean squared velocity averaged over the entire length of the 1-D array, which we present in Fig. 8. We find that the mean squared velocity grows with

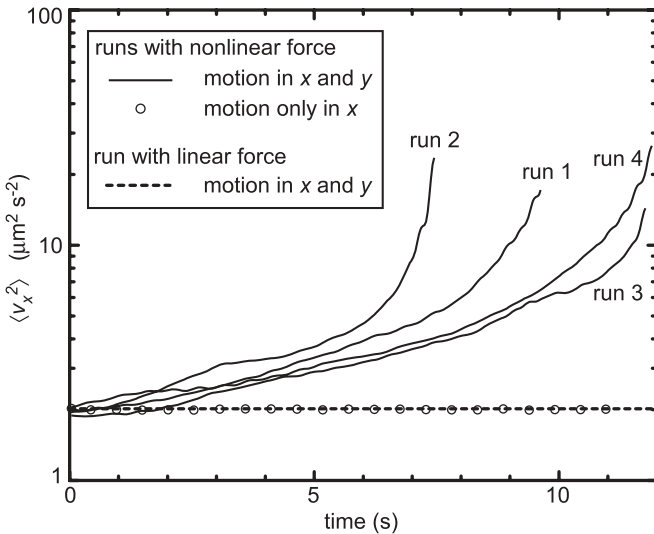


FIG. 8. Instability growth, as measured by the time series of the mean squared velocity, averaged over the entire length of the 1-D array. The simulation was run three ways for this test. The solid curves are four simulation runs for the fully nonlinear case using Eq. (3) when integrating the equation of motion, as in Figs. (1)–(6). The dashed curve is for the linear case using Eq. (4). The open circles are results for the fully nonlinear simulation with droplets constrained to move only longitudinally (i.e., in the x direction). We find that for the nonlinear case there is rapid nonexponential growth, but for the other two cases there is no growth, indicating that the instability requires nonlinearity and transverse motion. All the data in other figures of this paper are from run 1.

time, but unlike some hydrodynamic instabilities such as the Rayleigh-Taylor instability, this one has a growth that is not exponential with time. As a test, we verified by performing additional simulation runs that this nonexponential growth occurs regardless of the random initial positions that are chosen to start the simulation.

2. Spatial localization

In addition to its temporal dependence, we can also characterize the spatial dependence of the instability's growth. This can be examined in the spacetime diagram, Fig. 6. We find that the instability does not grow uniformly along the entire length of the 1-D array, but instead it develops in the form of isolated fluctuations. An example of this spatial concentration is seen prominently at $t > 8$ s, as marked * in Fig. 6(b). This large-amplitude disturbance is highly localized, with a width of $3a$ to $4a$ (i.e., it includes only three or four droplets). This width is consistent with the experimental observation of a fluctuation of $1 + 3$ droplets [6,8].

We note that the spatial width of $\approx 4a$ of this disturbance corresponds to a wave number of $ka \approx \pi/2$. In the wave spectra, this same wave number of $\pi/2$ was found to have a concentration of spectral power. Thus, we can suggest that the concentration of spectral power that is seen in the wave spectra is due to the spatial localization of the wave's growth.

3. Requirement of nonlinearity

We perform a test to assess the role of nonlinearities in the instability's growth. We do this by comparing results for the simulation run with different expressions for the potential: for the fully nonlinear run we use Eq. (3), while for the linear run we use Eq. (4) and retain only the first four terms on the right-hand side of Eq. (4).

Results in Fig. 8 show that there is no growth of the mean squared velocity of the droplets when nonlinearities are turned off. Thus, we can conclude that the instability requires nonlinearities in the potential. This conclusion confirms the suggestion of the experimenters [6,8] that the instability is essentially the result of a nonlinearity. This result is not surprising because a dispersion relation derived by linearizing the forces is purely real, with $\text{Im}[\omega(k)] = 0$ for all k [6].

4. Requirement of transverse motion

We perform another test to confirm that motion in the longitudinal direction cannot grow due to an instability in the absence of transverse motion. We expect that transverse motion is required, according to Beatus *et al.* [8], who showed that the instability can arise from the coupling between a transverse zigzag and a longitudinal pairing mode. In our test, we constrain the droplets to move only along the x axis by loading the simulation with nonzero initial displacements only in the x direction. Otherwise, the simulation in this test was the same as for our other fully nonlinear ones.

Results, shown with the open circles in Fig. 8, indicate no growth when the droplets are constrained to move only along the x axis. This finding confirms that the instability requires transverse motion.

Considering that all low-amplitude fluctuations can be decomposed as a spectrum of longitudinal waves for motion

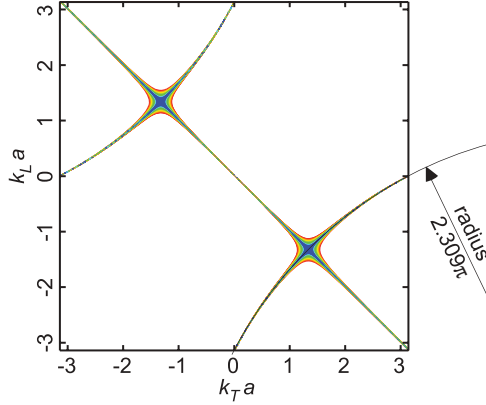


FIG. 9. (Color online) Contours of Δ as defined in Eq. (A1), assuming the dispersion relations in Eq. (7). Darker colors indicate smaller values of Δ . We find that the minima of these contours (the darkest colors) coincide with the dark features in Fig. 4, demonstrating that the matching criterion is modeled accurately by Eq. (14). A portion of a circle is shown, with a center at $(2.058\pi, -2.058\pi)$ and a radius of 2.309π , as determined by a manual fit. The agreement of this circle with the locus of the minima motivates the forms of Eqs. (15) and (16).

along the x axis and transverse waves for motion in the y direction, it is reasonable to conclude that the instability involves a coupling between longitudinal and transverse waves. Moreover, combining this conclusion with the previous one for nonlinearity, we have confirmed the suggestion of Beatus *et al.* that *the instability involves an interaction of the longitudinal and transverse waves*. While we have not determined the exact nature of this interaction, one possibility is the resonant wave interaction mechanism described in Sec. III B 1.

IV. SUMMARY

We performed a numerical simulation to study waves and an instability in a 1-D array of water droplets in a microfluidic channel. The droplets were modeled as point objects that interact with each other via a hydrodynamic potential. The oscillatory motion of the droplets, as characterized in the inertial frame of the droplets, exhibits two waves: a longitudinal wave that is backward with respect to the direction of oil flow, and a transverse wave that is forward. The simulation spectra for these waves agree well with the previous experiment that we simulate [6]. The droplet motion increases with time; this instability varies nonexponentially with time, and its growth is spatially localized. We performed two tests that confirm that the instability requires (1) nonlinearities in the hydrodynamic

potential and (2) an interaction between longitudinal and transverse waves. A possible candidate for this interaction is a nonlinear resonant wave interaction, which is suggested by a feature seen in our wave spectrum.

ACKNOWLEDGMENTS

The authors thank R. Bar-Ziv, T. Beatus, and T. Tlusty for helpful discussions. This work was supported by the NSF.

APPENDIX: DERIVATION OF MATCHING CONDITIONS FOR WAVE NUMBERS

We explain how we obtained the approximate expressions of Eqs. (15) and (16) for the matching conditions for wave numbers.

Our calculation involved three steps. First, we numerically found the wave numbers that satisfy the frequency matching condition Eq. (14). This was done by minimizing the difference

$$\Delta = |\omega_L(k_L) - \omega_T(k_T)| \quad (\text{A1})$$

over various combinations of k_L and k_T , where ω_L and ω_T are calculated using the dispersion relations in Eq. (7). We present the resulting contours of Δ in Fig. 9, which we examined to identify the curve representing the minima of $\Delta(k_L, k_T)$. Comparing Fig. 9 to Fig. 4, we found a coincidence of the regimes for the minima with those for the dark regions of high correlation in Fig. 4, which motivated the wave-number matching condition Eqs. (12) and (13). This coincidence indicates that the wave-number matching condition, as obtained from the correlation functions for waves, can be obtained from the frequency matching condition.

Second, we empirically obtained a formula that can describe the shapes of the regime of k_L and k_T where Δ has a minimum. In Fig. 9, we found that the equation of a circle accurately matches the shape of the minima of Δ . By varying the radius and center of the circle to obtain a visual fit, we found

$$k_L a = -\sqrt{(2.309\pi)^2 - (k_T a + 2.058)^2} + 2.058\pi \quad (\text{A2})$$

for $-\pi \leq k_T a \leq 0$, and

$$k_L a = \sqrt{(2.309\pi)^2 - (k_T a - 2.058)^2} - 2.058\pi \quad (\text{A3})$$

for $0 \leq k_T a \leq \pi$.

Finally, we calculated $\epsilon(k_T) = -k_L a + k_T a + \pi$ using Eq. (A2) for $-\pi \leq k_T a \leq 0$, and $\epsilon(k_T) = k_L a - k_T a + \pi$ using Eq. (A3) for $0 \leq k_T a \leq \pi$. This calculation yielded the approximate expressions for ϵ , as presented in Eqs. (15) and (16).

-
- [1] G. M. Whitesides, *Nature (London)* **442**, 368 (2006).
 [2] Tsevi Beatus (private communication).
 [3] B. Zheng, J. D. Tice, and R. F. Ismagilov, *Adv. Mater.* **16**, 1365 (2004).
 [4] R. R. Pompano, W. Liu, W. Du, and R. F. Ismagilov, *Annu. Rev. Anal. Chem.* **4**, 59 (2011).

- [5] N. Champagne, E. Lauga, and D. Bartolo, *Soft Matter* **7**, 11082 (2011).
 [6] T. Beatus, T. Tlusty, and R. Bar-Ziv, *Nat. Phys.* **2**, 743 (2006).
 [7] T. Beatus, R. Bar-Ziv, and T. Tlusty, *Phys. Rev. Lett.* **99**, 124502 (2007).
 [8] T. Beatus, R. Bar-Ziv, and T. Tlusty, *Phys. Rep.* **516**, 103 (2012).

- [9] C. Simonnet and A. Groisman, *Anal. Chem.* **78**, 5653 (2006).
- [10] M. T. Sullivan, K. Moore, and H. A. Stone, *Phys. Rev. Lett.* **101**, 244503 (2008).
- [11] T. Thorsen, R. W. Roberts, F. H. Arnold, and S. R. Quake, *Phys. Rev. Lett.* **86**, 4163 (2001).
- [12] P. Garstecki and G. M. Whitesides, *Phys. Rev. Lett.* **97**, 024503 (2006).
- [13] W. Lee, H. Amini, H. A. Stone, and D. D. Carlo, *Proc. Natl. Acad. Sci. USA* **107**, 22413 (2010).
- [14] M. Baron, J. Blawdziewicz, and E. Wajnryb, *Phys. Rev. Lett.* **100**, 174502 (2008).
- [15] M. Polin, D. G. Grier, and S. R. Quake, *Phys. Rev. Lett.* **96**, 088101 (2006).
- [16] B. Liu, K. Avinash, and J. Goree, *Phys. Rev. Lett.* **91**, 255003 (2003).
- [17] T. E. Sheridan, *Phys. Scr.* **80**, 065502 (2009).
- [18] J. V. Pearce, M. A. Adams, O. E. Vilches, M. R. Johnson, and H. R. Glyde, *Phys. Rev. Lett.* **95**, 185302 (2005).
- [19] M. P. Allen and D. J. Tildesley, *Computer Simulation of Liquids* (Oxford University Press, New York, 1989).
- [20] C. K. Birdsall and A. B. Langdon, *Plasma Physics via Computer Simulation* (Adam Hilger, New York, 1991).
- [21] W. H. Press, A. A. Teukolsky, W. T. Vetterling, and B. P. Flannery, *The Art of Scientific Computing*, 2nd ed. (Cambridge University Press, New York, 1992), p. 704.
- [22] In a test, we varied the standard deviation (i.e., the amplitude of the initial random displacements) to verify that our main results were not sensitive to it. As expected, the only effect was a trend of hastening the onset of the instability when a larger standard deviation was chosen.
- [23] J.-P. Hansen and I. R. McDonald, *Theory of Simple Liquids*, 2nd ed. (Elsevier Academic Press, San Diego, 1986), p. 214.
- [24] See Supplemental Material at <http://link.aps.org/supplemental/10.1103/PhysRevE.86.046309> for a movie of droplet motion.
- [25] P. G. Drazin and W. H. Reid, *Hydrodynamic Stability*, 2nd ed. (Cambridge University Press, New York, 2004), p. 392.
- [26] F. F. Chen, *Introduction to Plasma Physics and Controlled Fusion*, 2nd ed. (Plenum Press, New York, 1984), p. 309.
- [27] R. W. Boyd, *Nonlinear Optics*, 2nd ed. (Academic Press, San Diego, 2003), p. 78.